RESEARCH ARTICLE

LASER & PHOTONICS REVIEWS

www.lpr-journal.org

Vortex Beam Lasing from III-V Nanowires Epitaxially Grown on Silicon-on-Insulator

Bogdan-Petrin Ratiu, Ji Tong Wang, Kyle Netherwood, Tim Grieb, Andreas Rosenauer, Sang Soon Oh, Nicolae-Coriolan Panoiu,* and Qiang Li**

Photonic crystal lasers can be used to achieve high emission powers with exceptional beam quality. Vortex beams carrying orbital angular momentum have found applications in areas such as free space communication, optical trapping, and microscopy. In this paper, the growth and operation of an epitaxially grown InGaAs nanowire photonic crystal laser on silicon on insulator, emitting a vortex beam, are investigated. The device is composed of a honeycomb array of nanowires, with compressed and expanded configurations to make use of the band inversion phenomenon. The resulting bound-state-in-the-continuum modes are characterized using simulations and confirmed by measurement.

1. Introduction

Photonic crystal (PhC) lasers have been widely studied due to their many advantages, including high power operation,[1,2] high efficiency,[3,4] excellent beam quality,[5] and beam shaping properties.[5,6] These properties make PhC lasers good candidates for many applications, including optical communication,[6] laser machining,[7] light detection and ranging (LIDAR),[8] and sensing.[9] Lately, bound-state-in-the-continuum (BIC) lasers have gained attention due to their vertical emission of vortex beams with nonzero orbital angular momentum (OAM).[10–14]

A vortex beam, compared to the more standard Gaussian beams, is a structured form of light with varying amplitude, phase and polarization.[15] The donut-shaped intensity distribution of the beam has been used to increase the resolution of optical microscopes.[16,17] The spatially varying polarization of the beam can increase the efficiency of optical tweezers[18] and increase the absorption of light used for laser machining.[7] Vortex beams also have advantages for free-space communication, ranging and sensing due to their robustness against atmospheric turbulence.[6,8,19] In terms of optical fiber communication, vortex beams provide an additional degree of freedom in space-division multiplexing applications[19,20] due to their topological charge.

The generation of vortex beams was previously achieved using traditional optics components.[21,22] In recent years, metasurfaces,[21–24] vertical cavity surface emitting lasers, and PhCs[25–28] have been studied as methods of generating vortex beams, which have the advantages of miniaturization and ease of fabrication. Most of these results were based on top-down approaches. Metasurfaces can create arbitrary shaped beams, including OAM-carrying vortex beams. External metasurfaces can achieve high efficiencies,[24] but require external light sources as well as the use of free-space optical setups. On-chip generation can be achieved using spiral staircase structures,[29] corrugated waveguides,[30] or metasurfaces.[31] However, all these techniques require an external laser and suffer from comparatively low scattering efficiencies, generally under 15%.

Selective area epitaxy of nanowires provides a versatile platform for bottom-up PhC lasers with expanded design space. Additionally, nanowires can elastically relax the stress caused by lattice and thermal mismatch without the creation of threading dislocations.[32] There is an exciting prospect of epitaxially integrating a laser source on silicon wafers for use in silicon photonics. Recent advances in silicon photonics have made it possible to couple light from photonic crystal surface-emitting lasers into waveguides,[33] transmit light through OAM-maintaining waveguides,[34] as well as OAM-based multiplexing and demultiplexing.[35,36] These advancements highlight the possibility of exploiting the additional degree of freedom of OAM to increase optical communication bandwidths, as well as the necessity of an integrated OAM-producing light source.

B.-P. Ratiu, K. Netherwood, S. S. Oh, Q. Li
School of Physics and Astronomy
Cardiff University
Cardiff CF10 3AT, UK
E-mail: OhS2@cardiff.ac.uk; liq44@cardiff.ac.uk

J. T. Wang, N.-C. Panoiu
Department of Electronic & Electrical Engineering
University College London
London WC1E 6BT, UK
E-mail: n.panoiu@ucl.ac.uk

T. Grieb, A. Rosenauer
Institute of Solid State Physics
University of Bremen
28359 Bremen, Germany

The ORCID identification number(s) for the author(s) of this article can be found under https://doi.org/10.1002/lpor.202501297

DOI: 10.1002/lpor.202501297

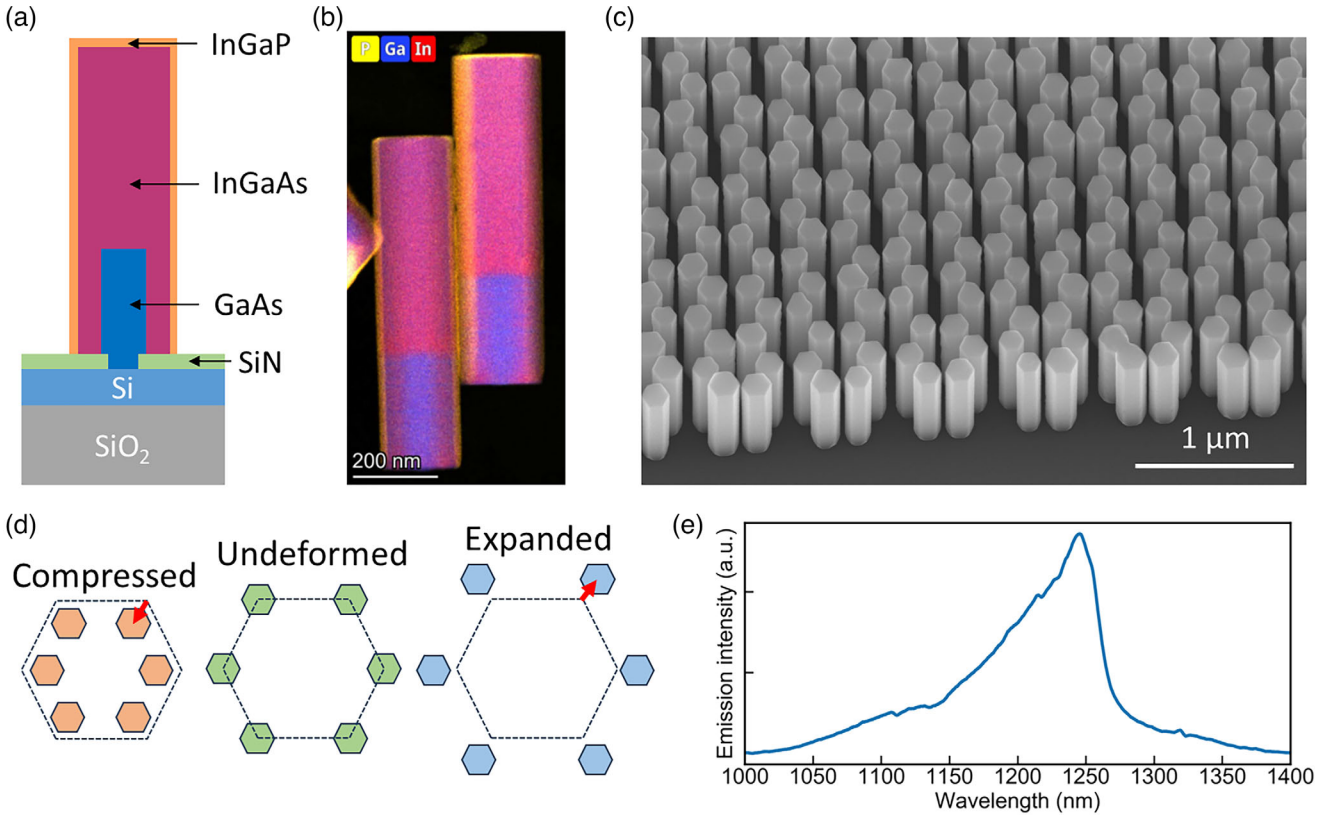

Figure 1. InGaAs nanowire array characterization. a) Cross-section diagram of the nanowire. b) Elemental mapping of the nanowires. c) Tilted SEM image of the as-grown nanowire array. d) Diagram of the honeycomb unit cell showing the positions of the nanowires in compressed, undeformed, and expanded arrays. e) Photoluminescence spectrum of the InGaAs nanowires.

In this work, we present the growth and operation of an epitaxially grown InGaAs nanowire photonic crystal laser on silicon-on-insulator (SOI). By deforming the honeycomb lattice, we take advantage of the band inversion effect to shift the high-quality (Q)-factor quadrupole mode to match the gain material emitting at the telecom O-band wavelength. Simulations show the quadrupole mode is a symmetry-protected BIC mode, emitting a donut-shaped beam with a topological charge of −2. Measurements of the far-field emission pattern and photonic band structure confirm the topological charge and band inversion effect, showing the suitability of this approach for applications in the areas of optical communications, optical trapping, high-resolution imaging and LIDAR.

2. Results

The nanowire array was epitaxially grown on a patterned SOI substrate with the silicon device layer oriented in the (111) direction. **Figure** 1a shows a cross-sectional diagram of the design configuration of the nanowire. The buried oxide layer helps confine the mode to the nanowires due to its lower refractive index. To prevent the mode leaking into the (111) silicon layer,[37] the thickness of the silicon was reduced to 52 nm. A SiN layer was deposited as the hard mask for the selective area epitaxy. Electron-beam lithography was used to etch SiN to open circular holes with diameters from 30 to 80 nm and expose the silicon layer for nanowire nucleation. The initial nanohole patterns were arranged in undeformed, compressed and expanded honeycomb arrays with a fixed lattice constant of 640 nm. The unit cells are schematically represented in Figure 1d. The inner hexagon radius R is 210, 200, and 230 nm for the undeformed, compressed, and expanded honeycomb patterns, respectively.

The MOCVD growth begins with a GaAs layer, which serves two purposes: improving the yield, uniformity, and aspect ratio of the nanowires, as well as elevating the optical mode away from the (111) silicon layer due to the refractive index contrast. The optical mode is largely confined to the InGaAs layer, which provides gain in the telecom O-band region, as shown in Figure 1e. The conformal InGaP shell surrounding the nanowires reduces the impact of surface nonradiative recombination centers.[38] The highest yield was achieved from 30 nm diameter nanohole arrays. At larger hole sizes, the nanowires tended to merge together due to the considerable lateral growth. The details of the fabrication and epitaxy processes can be found in the Materials and Methods section.

To confirm the structure of nanowires, the nanowires were transferred to a transmission electron microscope (TEM) grid and measured using Energy Dispersive X-ray Spectrometry (EDX). Figure 1b shows the elemental mapping with phosphorus, gallium and indium highlighted. The comparatively Ga-rich GaAs core is visible on the bottom of the nanowire. The pink In-rich InGaAs region around the core shows radial growth around the core. The main axially grown bulk of the nanowire shows a relatively uniform InGaAs composition. The yellow

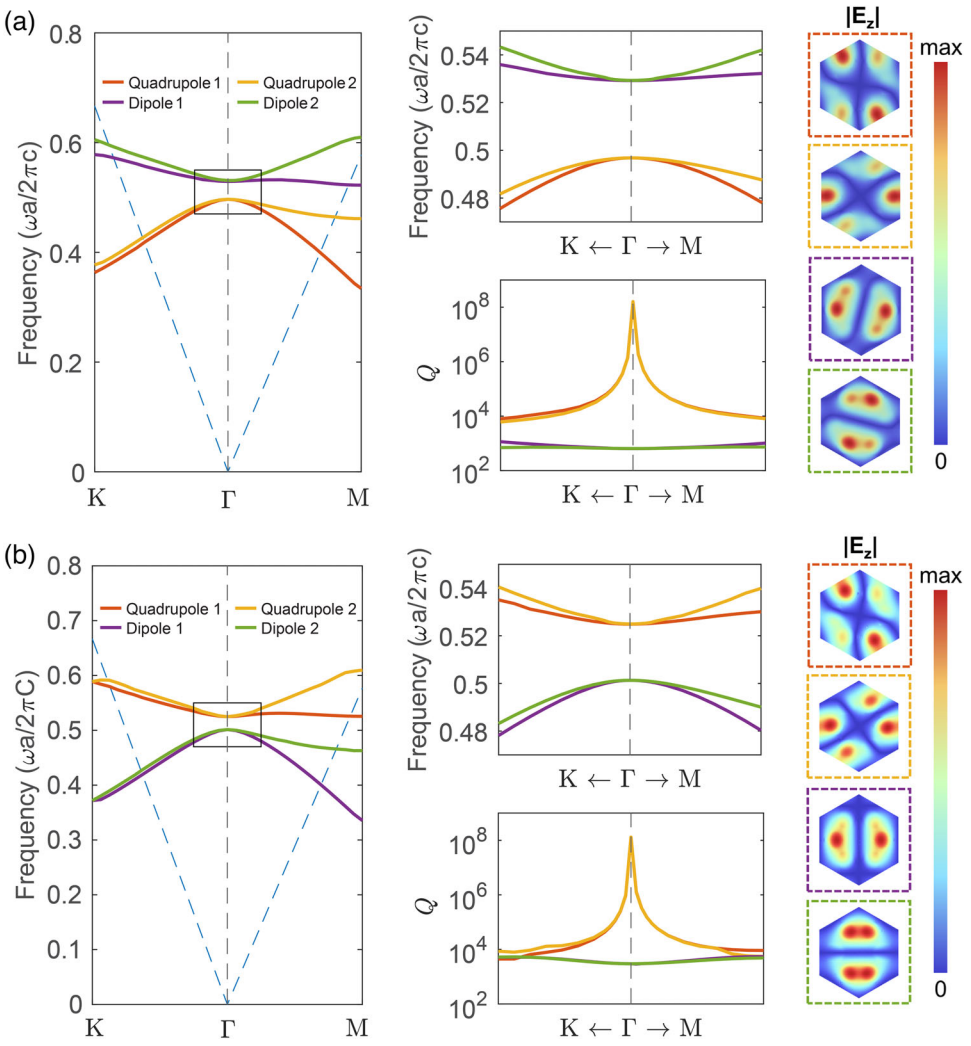

Figure 2. Band structure and eigenmode analysis for expanded and compressed nanowire arrays. a) Numerical investigation of the expanded lattice (R = 230 nm). Left panel, band structure along K – Γ – M directions, where the light blue dashed line denotes the light line $\omega = ck_{||}$ and $k_{||}$ is the in-plane Bloch wavevector. Top middle panel, zoom-in band structure corresponding to the rectangular frame in the left panel. Bottom middle panel, Q-factor plots of the four eigenmodes along the selected wavevector path. Right panel, distribution of the electric field $|E_z|$ of the quadrupole and dipole modes at the Γ-point in the middle plane of the nanowire structure. b) The same as in a, but for the compressed lattice (R = 200 nm).

P-rich regions show that the InGaP shell conformally covers the entire surface of the nanowire. Additional high-resolution TEM images of the GaAs/InGaAs interface can be found in Figure S14 (Supporting Information), confirming the lack of threading dislocations despite the lattice mismatch.

A typical expanded nanowire array with a hole diameter of 30 nm is shown in Figure 1c. The nanowire diameter is 160 nm with a variance of 6%. The average height is ≈630 nm. The yield of individual nanowires is almost 100% with very few nanowires merged or missing. Hole diameters of 40, 50, and 60 nm still show high yield, but the density of defect nanowires increases.

2.1. Theory and Simulation

To demonstrate the underlying physics of the band inversion phenomena introduced by deforming the honeycomb lattice, we considered the photonic band structure and eigenmode analysis of the infinite-size structure for both expanded (R = 230 nm, **Figure** 2a) and compressed (R = 200 nm, Figure 2b) nanowire arrays. The calculations were performed using the finite-element method implemented in COMSOL Multiphysics.[39] Due to the nature of the structure deformation and differences in intra- and inter-cell mode coupling intensity,[40,41] the degenerate quadrupole pair of modes has lower frequency in the expanded case, whereas the pair of dipole modes has lower frequency in the compressed case, indicating the inversion of the band structure. In both cases, the nanowire array supports a band gap, as per Figures S5 and S6 (Supporting Information), which closes in the case of an undeformed array (see Figure S3a, Supporting Information) due to the existence of doubly degenerate Dirac cones at the Γ-point formed by the fold-back of Dirac cones at the K and K' symmetry points.

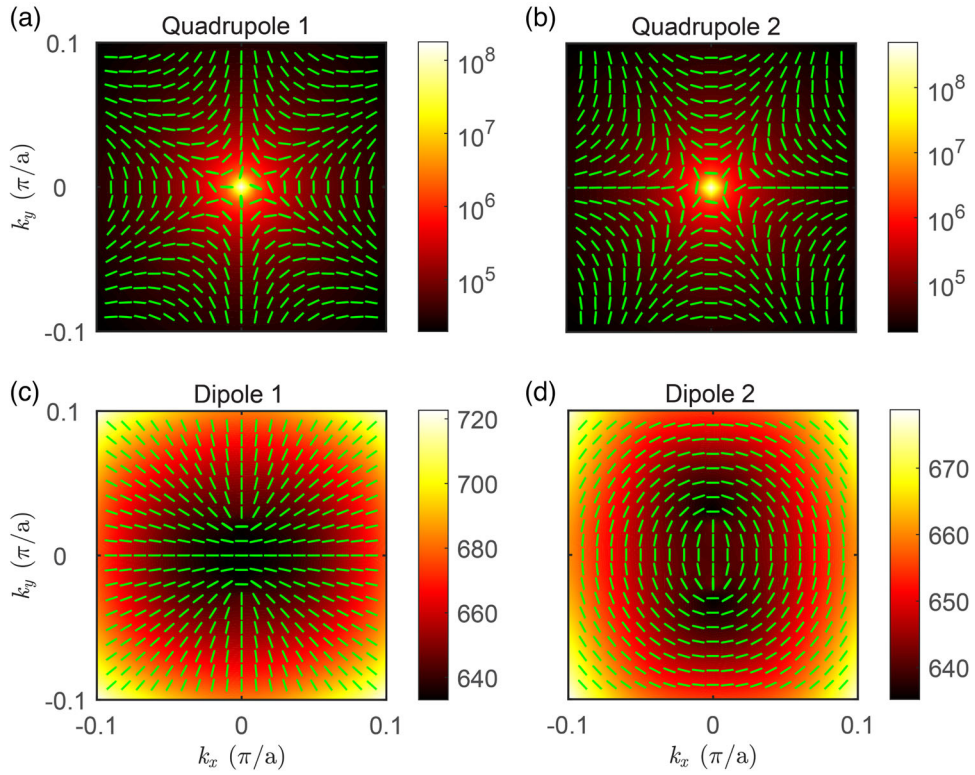

Figure 3. Numerically calculated radiative Q-factor map and far-field polarization of the four modes of the expanded lattice. a) Quadrupole 1. b) Quadrupole 2. c) Dipole 1. d) Dipole 2. For the quadrupole pair, Q-factor maps are plotted using a base-10 logarithmic scale, while those of the dipole pair are displayed in a linear scale. The short green dashes denote the direction of the electric far-field polarization at a series of k-points.

It should be noted that the Q-factors of the two quadrupole modes diverge to infinity at the Γ-point for both expanded and compressed structures, suggesting that they are symmetry-protected BICs. By contrast, the Q-factors of the two dipole modes are almost constant around the Γ-point, i.e., $\approx 10^3$ ($\approx 10^4$) for the expanded (compressed) array. Moreover, if the honeycomb nanowire array has R = a/3 (undeformed), the two dipole modes become accidental BICs with infinite radiative Q-factor at the Γ-point (see Figure S3b, Supporting Information).

We also studied the scaling properties of the radiative Q-factor of the pair of quadrupole modes (symmetry-protected BICs) along ΓM and ΓK directions (see Figure S4, Supporting Information). The results demonstrate the inversely quadratic dependence of their radiative Q-factor on small wavevector displacement from the Γ-point.[13,42] Moreover, both quadrupole and dipole modes are found to be predominantly transverse-magnetic modes. The z-component of their electric field, computed in the middle of the nanowire structure, is presented in the right panels of Figure 2a,b.

To further investigate the topological nature of the degenerate modes as symmetry-protected BIC-type modes, we calculated their Q-factor and far-field polarization state in the k-space, in the case of the expanded array; the results of these calculations are summarized in **Figure 3**. In the case of the pair of quadrupole modes, their Q-factor drops rapidly away from the Γ-point, following an inversely quadratic scaling law. In addition, around the Γ-point, the far-field polarization states are almost linearly polarized and accumulate a -4π phase variation along a counterclockwise-oriented closed loop, indicating the topological charge,[38] q = −2. Note that the far-field polarization vector at the Γ-point is ill-defined because of the vanishingly small amount of radiative energy.

Moving now on to the pair of dipole modes, we see that their Q-factor varies only moderately in the vicinity of the Γ-point. Interestingly, despite their trivial topological properties at the Γ-point, one can still observe the winding features of the far-field polarization with phase accumulation of $+2\pi$, which can be explained by their quasi-BIC nature stemming from their BIC nature when the structure is undeformed (see Figure S3b, Supporting Information). That is to say, by slightly increasing R from 213 to 230 nm, one drastically changes the Q-factor, but the winding features of the far-field polarization nearby the Γ-point are preserved. We also investigate the Q-factor and far-field polarization properties for the compressed array, and similar conclusions are found, as can be seen in Figure S7 (Supporting Information).

2.2. Optical Characterization

To characterize the far-field emission properties, angle-resolved photoluminescence was used to measure the photonic band structure of the compressed and expanded arrays. **Figure 4** shows such a measurement for the compressed and expanded arrays in the M̄-Γ-M direction, at an excitation power close to the lasing threshold. The experimental details of the measurement can be found in Experimental Section. The spontaneous

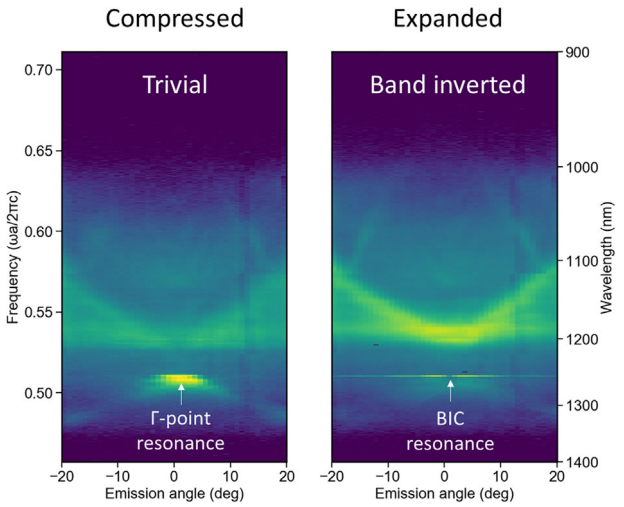

Figure 4. Angle-resolved photoluminescence band structure measurement pumped close to the lasing threshold. a) Compressed array b) Expanded array. The emission angle corresponds to the -M – Γ – M k-vector. The band inversion effect is seen in the expanded lattice, where the quadrupole BIC mode is on the lower band.

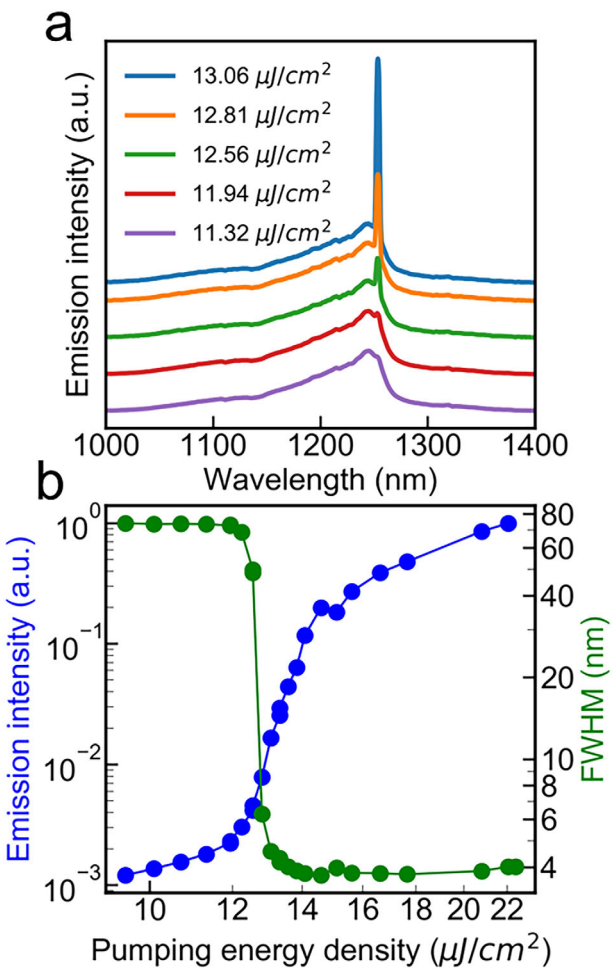

Figure 5. Optical characterization of a quadrupole lasing mode from an expanded lattice. a) Emission spectra at various pumping powers close to the lasing threshold. b) LL curve and FWHM for the lasing mode showing the typical S-curve shape.

emission is roughly uniform with respect to emission angle across the measurement range, while the amplified emission is dependent on the k-vector of the resonance, leading to a clear emission directionality. The resulting measurement reveals the emissive portions of the band structure. Both arrays show flat band edges at the Γ point, corresponding to a 0° emission angle. The BIC quadrupole mode does not couple with radiative waves at Γ, resulting in a dark spot at the band edge. In the compressed structure the quadrupole mode is on the higher band edge. Band inversion occurs in the expanded version, resulting in the quadrupole mode appearing at the lower band edge. Since the measurement is taken at close to the lasing threshold, we can see that the lasing resonance always occurs at the lower band edge, whether it is a dipole or quadrupole mode. This measurement of the band structure and band inversion correlates well with the simulated results shown in Figure 2.

Optical characterization of a typical quadrupole lasing peak under optical pumping is shown in **Figure 5**. The lasing peak remains single mode for all tested pumping powers due to the gain competition. The evolution of the emission spectrum around the threshold can be seen in Figure 5a. There is an excellent alignment between the BIC resonance wavelength and the peak of the gain material (Figure 1e). The lasing threshold pulse energy is 12.6 μJ cm^{-2}, or in terms of average power 12.6 W cm^{-2}. The light-light curve and full-width at half-maximum (FWHM) are depicted in Figure 5b, showing a clear lasing threshold. A narrowing of the emission spectrum is visible around the threshold, followed by a small increase in spectral FWHM with higher pump power.

The linewidth in Figure 5b is broadened by the experimental setup including a wide spectrometer slit along with the use of a low density grating of the spectrometer. The wide slit was required to image the 2D far field projection and the rotation due to polarization, which is to be discussed shortly. We have measured a high resolution spectrum from an expanded array, as shown in Figure S13 (Supporting Information). A linewidth of 0.227 nm was obtained just above the threshold, which can be used to calculate a Q factor of 5534. Using this, the cavity lifetime can be approximated to be ≈50 ps. Therefore, we expect the cavity is fully depleted in between the pulses, confirming the pulsed mode operation of the laser. The duration of the pumping pulse is 100 ps, roughly twice as long as the cavity lifetime, which is likely enough time for a reasonably stable carrier steady state to form.

The far-field lasing pattern can be seen in **Figure 6**. The lack of lasing emission at the center of the beam, corresponding to the Γ point, confirms that the mode is a BIC state. The beam shape is roughly donut-shaped. A linear polarizer is used to measure the polarization state of the laser beam. A four-lobed pattern is observed for all polarization angles. The pattern rotates as the polarizer angle changes. The pattern rotates −45° for a 90° rotation of the polarizer, which is consistent with a topological charge of −2 as found from simulations. The divergence angle of the beam is ≈14°. By comparing the measured polarizer-resolved far-field intensity profiles shown in Figure 6 with the simulated far-field polarization maps of the two quadrupole modes presented in

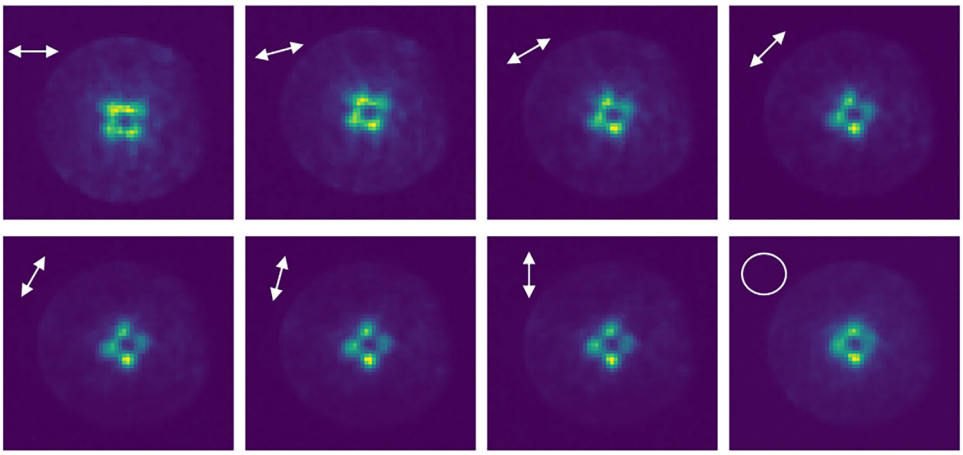

Figure 6. Far field lasing pattern polarization dependence for an expanded lattice. The arrows represent the polarizer direction, with images taken in 15° steps. The circle represents measurement with no polarizer. The rotation of the far field pattern reveals a topological charge of −2.

Figure 3a,b, it can be seen that quadrupole 1 mode is the lasing BIC mode. The far field profile and polarization dependence of the dipole mode in the compressed lattice can be seen in Figure S1 (Supporting Information). It shows a narrow, linearly polarized beam with Γ-point emission, as predicted by the simulations presented in Figure S7 (Supporting Information).

In addition to the simulation of infinite-size nanowire arrays, implemented using a procedure based on a unit cell with Bloch periodic boundary conditions, we also carried out the simulation of finite-size hexagonal arrays with a side length of N = 9 nanowires, as per Figures S8–S11 (Supporting Information). The finite-size simulation results demonstrate that the pair of quadrupole modes generates vortex far-field beams with donut-shape profiles, which is explained by the nonradiative property of the symmetry-protected BICs at the Γ-point. By contrast, the far-field patterns corresponding to the pair of dipole modes have no vortex-like features. Interestingly, our finite-size calculations show that the far-field emitted from the pair of quadrupole modes is characterized by a topological charge, $q = -1$, which is different from the infinite-size simulation. To understand this finding, one should approximate the wave solutions of finite-size photonic structures to the product between infinite Bloch functions and envelope functions.[43,44] Under this approximation, the envelope functions might modify the symmetry properties of the overall solution and thus the topological properties of the solutions corresponding to finite structures. Similar conclusions have been recently reported.[38] As the number of nanowires in the finite structure increases, one expects that the finite-size structures begin to support optical modes with topological charge $q = -2$.

2.3. Influence of Defects

While the study of random lasers is now a mature area of laser science,[45,46] it mostly focuses on randomly positioned optical wave scatterers. The impact of random perturbations in the size of holes or pillars of PhC arrays is studied to a lesser extent.[47] Here, we experimentally study the effect of random defects in the nanowire array on the lasing threshold by using devices with different nanohole sizes.

The most common type of defect in the arrays is the merging of two nanowires into a nanofin-like structure. An additional source of random perturbation is the nanowire diameter variation. As the nanowire size increases, the likelihood of merging increases. Additionally, the diameter distribution narrows, as some of the larger nanowires merge together to form fins. The band structures of arrays with increasing defect densities can be seen in Figure S2 (Supporting Information). The photonic crystal bands can still be observed even at high defect densities, though the resonance strength decreases.

The impact of these defects on the lasing threshold is illustrated in **Figure 7**. As expected, an increase in defect density leads to an increase in lasing threshold. Interestingly, the compressed and expanded arrays show different dependence on the defect density, namely, it has a much lower impact on the compressed array (dipole mode) than on the expanded array (quadrupole mode).

Additionally, several other effects should be considered when comparing samples with different nanohole sizes. First, the defect densities and size distributions can be visualized as a histogram (Figure 7b). Merged nanowires appear as a second peak, at roughly twice the area of a single nanowire. The ratio between these two peaks quantifies the defect density. Second, an increase in nanohole size leads to a slight increase in nanowire diameter, resulting in an increase in effective refractive index.

The increase of the effective refractive index induces a redshift of the resonance wavelength, which reduces the spectral overlap with the material gain. This leads to an increase in lasing threshold; however, this change affects the dipole and quadrupole modes in a similar way, so it cannot fully explain the difference shown in Figure 7a. The defect density has been found to correlate well with the lasing threshold. This suggests that the two optical modes are intrinsically affected in different manners by the structural disorder caused by fabrication defects.

This difference could be explained by the maps of Q factor as a function of k-vector shown in Figure 3 and Figure S7 (Supporting Information), showing the expanded and compressed arrays,

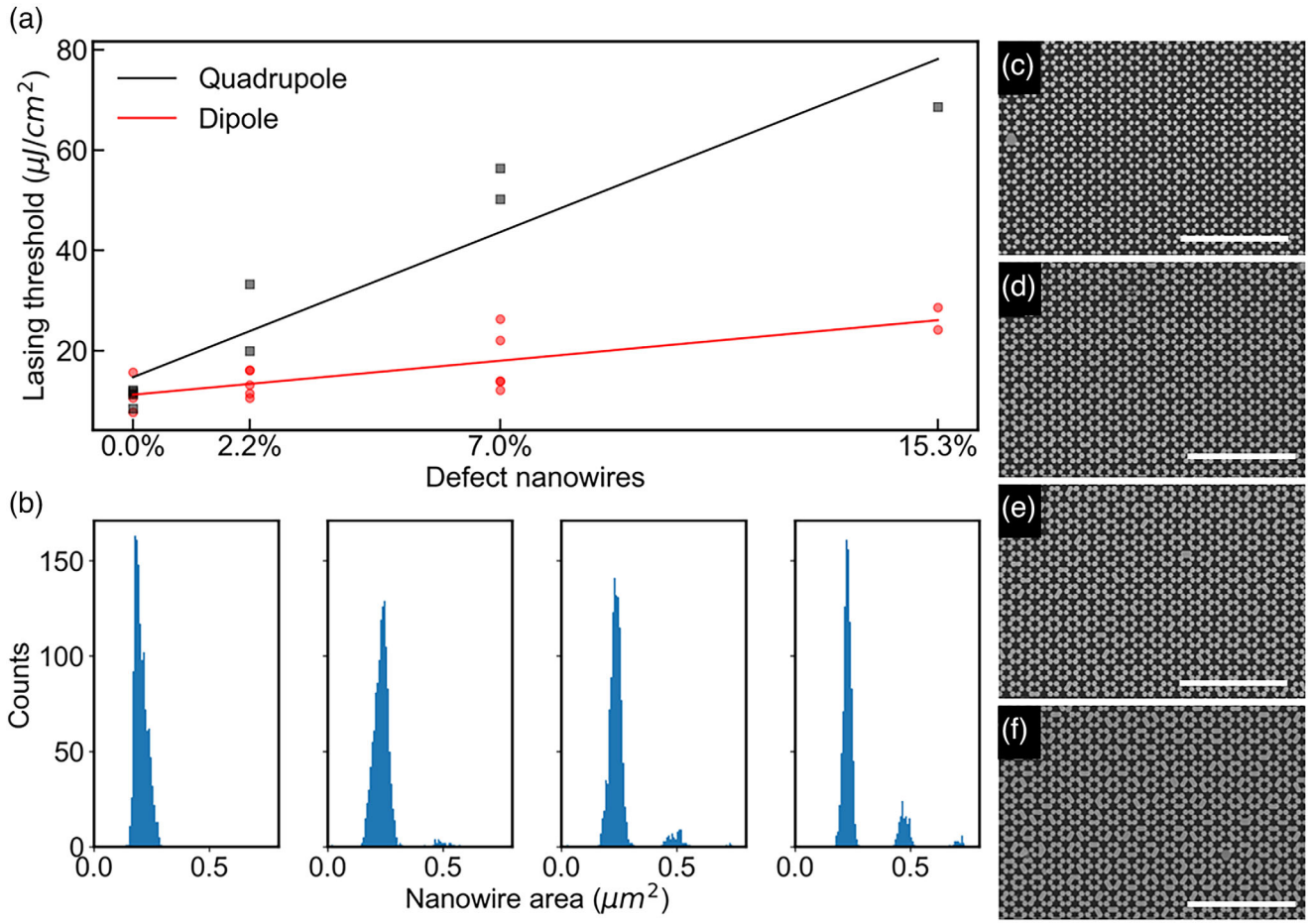

Figure 7. Effect of lattice defects on the lasing threshold. a) Laser threshold of different devices with different defect densities, with linear fits to show the trends. b) Histograms of nanowire area for each device, showing an increasing number of merged nanowire defects. c–f) SEM images of the devices with different defect densities. The scale bar is 4 µm.

respectively. For both array types, the quadrupole mode has a steep decline in Q factor away from the Γ-point, while the dipole mode is almost constant. This means that a small shift away from the Γ-point, such as one caused by a defect, will have a significantly greater impact on quadrupole modes compared to dipole modes, potentially explaining the difference in slope shown in Figure 7.

3. Discussion

In this paper, we have successfully demonstrated the growth and operation of an InGaAs nanowire photonic crystal laser on silicon-on-insulator that emits a vortex beam with a topological charge of −2. By employing a hexagonal nanowire array with lattice deformations, we leveraged bound states in the continuum at the optical band edges to achieve single-mode laser emission. Numerical simulations were carried out to understand and characterize the optical properties of the fabricated device. Experimental characterization confirmed the simulation results by measuring the photonic band structure and far-field emission.

The ability to directly integrate a III-V semiconductor nanowire laser onto a silicon platform creates new opportunities for implementing vortex beam sources in silicon photonic integrated circuits. Our approach produces a laser, which inherently creates a vortex beam, leading to a 100% scattering efficiency. Being an on-chip device, we bypass the need for free-space optics required for other methods. However, compared to the previous methods, the main limitation of our approach is the lack of flexibility in terms of the OAM produced. While spiral staircases and metasurfaces can create many angular momentum states, our approach can only create two states, 0 and −2, by expanding and contracting the photonic crystal lattice.

Dynamically tuning the OAM of the emitted beam would be an important step toward applications in communications. Our design relies on the BIC state to produce a beam carrying OAM. By breaking the BIC condition, we could modulate the laser both in terms of OAM, switching from −2 to 0, as well as spatially, switching between a donut-shaped beam to a Gaussian beam.

Making use of the thermo-optic effect to locally change the refractive index, therefore break the BIC symmetry, could potentially show good results for our device, due to the thermally insulating oxide layer beneath the nanowires.

Dynamically changing between a compressed and an expanded lattice is also an interesting potential future development. This might be achieved by starting with an undeformed lattice encased in an insulating material. This matrix could then be mechanically compressed or stretched using MEMS techniques or piezoelectric crystals.

4. Experimental Section

Fabrication: The nanowires were grown using selective-area metalorganic vapor phase epitaxy on a commercially available silicon-on-insulator substrate. The substrate has a (111) oriented silicon top layer, which was thinned to a thickness of 52 nm, and a 2-µm thick buried oxide layer. A 20 nm silicon nitride layer was deposited using plasma-enhanced chemical vapor deposition to serve as a growth mask. This layer was patterned using electron-beam lithography and etched to expose the (111) silicon surface in circular nanoholes with diameters of 30, 40, 50, and 60 nm. These nanoholes were arranged into undeformed, stretched, and compressed honeycomb lattices.

Before the nanowire growth, the patterned substrate underwent cleaning with a 2.5% diluted hydrofluoric acid solution for 10 min to remove native silicon oxide. The substrate was then transferred into an Aixtron Close Coupled Showerhead MOCVD reactor. A thermal desorption step was performed at 850 °C for 20 min under hydrogen flow to eliminate any residual oxide and prepare the silicon surface for III-V nucleation. The growth process began with the deposition of a GaAs core nanowire at 680 °C under a V/III ratio of 82. The temperature was reduced to 610 °C to grow the InGaAs layer with a V/III ratio of 40 and an In/III vapor supply of 40%. Finally, a lattice-matched 15 nm InGaP shell was grown at 570 °C.

Measurement: The optical micro-photoluminescence measurements were performed at room temperature. A pulsed supercontinuum laser source (YSL SC-PRO 7), filtered using a tunable wavelength filter (AOTF-Pro), was used to emit 100 ps pulses with a 1 MHz repetition rate at a wavelength of 633 nm. This pump light was focused using a 50× infinity-corrected objective lens (50× Mitutoyo Plan Apo NIR) onto the sample surface. The sample was intentionally defocused, leading to a pump beam with a diameter of ≈30 µm. The large optically pumped area and the pulsed nature of the laser help prevent thermal damage to the sample. The infrared PL emission is collected and collimated by the same lens. A lens is placed in front of the spectrometer (Acton Spectra Ro SP-2750) slit, so that the back focal plane is imaged onto the 2D array detector (NIRvana 640). An open slit was used to increase the measurement speed, leading to an artificial broadening of the spectrum. By imaging the zeroth-order diffraction of the grating, the detector simply acts as an infrared camera. By imaging the first-order diffraction beam, the spectral information can be collected.

The back focal plane of a lens translates the angle of propagation of a beam to spatial information, allowing us to measure the far-field emission pattern. The maximum acceptance angle of the lens, as given by the numerical aperture (NA = 0.65), was used to calibrate the measurement. In the far-field, each point corresponds to an emission direction, therefore to a k-vector of light. To measure the photonic band structure, the sample was aligned to the Γ-M k-vector emission. To reject other emission angles, the spectrometer slit was narrowed around the Γ-M direction.

Numerical Simulations: The COMSOL Multiphysics was used to numerically simulate both infinite- and finite-size nanowire arrays. For simplicity, the InGaP shells were merged with the InGaAs nanowire cores because they are very thin, and the two optical materials have roughly the same index of refraction. In addition, the penetration depth of GaAs core nanowire into the thin SiN layer was neglected. The refractive index of the materials from which the array of nanowires is made of was chosen to: 3.62 for InGaAs,[48,49] 3.4 for GaAs,[50] 2 for SiN,[51] 3.5 for Si,[52] and 1.45 for SiO_2.[53] The refractive indices of materials used in simulations are chosen based on the experimentally measured data at the device's lasing wavelength (≈1258 nm). In all cases, the absorption and dispersion are neglected due to the small extinction coefficients and weak dispersion over the studied spectrum range. The composition of InGaAs was found using energy dispersive X-ray spectroscopy.[4]

For the calculation of photonic band structure and eigenmode analysis corresponding to the infinite-size structures, a unit cell with Bloch periodic boundary conditions in the transverse plane was used, and layers applied along the *z*-axis were perfectly matched. The Q-factor was extracted from the complex-valued frequency of the corresponding optical modes, and the far-field polarization was determined from the zeroth-order Fourier component of the optical far-field.

For the simulation of finite-size structures, perfectly matched layers were applied as boundary conditions along all directions. The far-field patterns were determined by selectively propagating the nonevanescent (propagating) field components into the far-field region. Finally, the propagating wave components were extracted from the optical near-field calculated just above the nanowire structure.

Supporting Information

Supporting Information is available from the Wiley Online Library or from the author.

Acknowledgements

B-P.R. and J.T.W. contributed equally to this work. This work was supported by the Engineering and Physical Sciences Research Council (Grant Nos. EP/T01105X/1 and EP/V029681/1). This research was undertaken using the supercomputing facilities at Cardiff University operated by Advanced Research Computing at Cardiff (ARCCA) on behalf of the Cardiff Supercomputing Facility and the HPC Wales and Supercomputing Wales (SCW) projects.

Conflict of Interest

The authors declare no conflict of interest.

Data Availability Statement

The data that support the findings of this study are available at the Cardiff University Data Repository at https://doi.org/10.17035/cardiff.29822129.

Keywords

lasers, MOCVD, nanowires, photonic crystals, vortex beams

Received: May 27, 2025
Revised: July 14, 2025
Published online:

[1] K. Hirose, Y. Liang, Y. Kurosaka, A. Watanabe, T. Sugiyama, S. Noda, *Nat. Photonics* **2014**, *8*, 406 .
[2] S. Noda, T. Inoue, M. Yoshida, J. Gelleta, M. D. Zoysa, K. Ishizaki, *Adv. Opt. Photonics* **2023**, *15*, 977.
[3] S. Matsuo, A. Shinya, T. Kakitsuka, K. Nozaki, T. Segawa, T. Sato, Y. Kawaguchi, M. Notomi, *Nat. Photonics* **2010**, *4*, 648.
[4] C. Messina, Y. Gong, O. Abouzaid, B.-P. Ratiu, T. Grieb, Z. Yan, A. Rosenauer, S. S. Oh, Q. Li, *Adv. Opt. Mater.* **2023**, *11*, 2201809.
[5] M. Yoshida, M. De Zoysa, K. Ishizaki, W. Kunishi, T. Inoue, K. Izumi, R. Hatsuda, S. Noda, *J. Phys. Photonics* **2021**, *3*, 022006.

[6] J. Wang, J. Liu, S. Li, Y. Zhao, J. Du, L. Zhu, *Nanophotonics* **2022**, *11*, 645.
[7] M. Meier, V. Romano, T. Feurer, *Appl. Phys. A* **2007**, *86*, 329.
[8] W. Cheng, J. W. Haus, Q. Zhan, in *Atmospheric Propagation of Electromagnetic Waves III*, Vol. *7200*, SPIE, Washington, USA **2009**, p. 22.
[9] M. Cheng, W. Jiang, L. Guo, J. Li, A. Forbes, *Light Sci. Appl.* **2025**, *14*, 4.
[10] L. Allen, M. W. Beijersbergen, R. J. C. Spreeuw, J. P. Woerdman, *Phys. Rev. A* **1992**, *45*, 8185.
[11] C. W. Hsu, B. Zhen, A. D. Stone, J. D. Joannopoulos, M. Soljačić, *Nat. Rev. Mater.* **2016**, *1*, 16048.
[12] A. Kodigala, T. Lepetit, Q. Gu, B. Bahari, Y. Fainman, B. Kanté, *Nature* **2017**, *541*, 196.
[13] M.-S. Hwang, H.-C. Lee, K.-H. Kim, K.-Y. Jeong, S.-H. Kwon, K. Koshelev, Y. Kivshar, H.-G. Park, *Nat. Commun.* **2021**, *12*, 4135.
[14] H. Zhong, Y. Yu, Z. Zheng, Z. Ding, X. Zhao, J. Yang, Y. Wei, Y. Chen, S. Yu, *Light Sci. Appl.* **2023**, *12*, 100.
[15] M. R. Dennis, K. O'Holleran, M. J. Padgett, in *Progress in Optics*, (Ed.: E. Wolf), Vol. *53*, Elsevier, Amsterdam, Netherlands **2009**, p. 293.
[16] R. Dorn, S. Quabis, G. Leuchs, *Phys. Rev. Lett.* **2003**, *91*, 233901.
[17] S. Quabis, R. Dorn, M. Eberler, O. Glöckl, G. Leuchs, *Opt. Commun.* **2000**, *179*, 1.
[18] Y. Yang, Y. Ren, M. Chen, Y. Arita, C. Rosales-Guzmán, *Adv. Photonics* **2021**, *3*, 034001.
[19] J. Wang, *Photonics Res.* **2016**, *4*, B14.
[20] J. Liu, J. Zhang, J. Liu, Z. Lin, Z. Li, Z. Lin, J. Zhang, C. Huang, S. Mo, L. Shen, S. Lin, Y. Chen, R. Gao, L. Zhang, X. Lan, X. Cai, Z. Li, S. Yu, *Light Sci. Appl.* **2022**, *11*, 202.
[21] A Review of Orbital Angular Momentum Vortex Beams Generation: From Traditional Methods to Metasurfaces, https://www.mdpi.com/2076-3417/10/3/1015.
[22] Y. Bai, H. Lv, X. Fu, Y. Yang, *Chin. Opt. Lett.* **2022**, *20*, 012601.
[23] Y. Bao, J. Ni, C.-W. Qiu, *Adv. Mater.* **2020**, *32*, 1905659.
[24] F. Yue, D. Wen, J. Xin, B. D. Gerardot, J. Li, X. Chen, *ACS Photonics* **2016**, *3*, 1558.
[25] L. Yang, G. Li, X. Gao, L. Lu, *Nat. Photonics* **2022**, *16*, 279.
[26] X. Gao, L. Yang, H. Lin, L. Zhang, J. Li, F. Bo, Z. Wang, L. Lu, *Nat. Nanotechnol.* **2020**, *15*, 1012.
[27] C.-J. Chang, Y.-W. Chen, L.-R. Chen, K.-B. Hong, J.-S. Wu, Y.-W. Huang, T.-C. Lu, *ACS Photonics* **2023**, *10*, 4112.
[28] K. Kitamura, M. Kitazawa, S. Noda, *Opt. Express* **2019**, *27*, 1045.
[29] H. Li, D. B. Phillips, X. Wang, Y.-L. D. Ho, L. Chen, X. Zhou, J. Zhu, S. Yu, X. Cai, *Optica* **2015**, *2*, 547.
[30] L. I. Bakirova, G. S. Voronkov, V. S. Lyubopytov, M. A. Butt, S. N. Khonina, I. V. Stepanov, E. P. Grakhova, R. V. Kutluyarov, *Micromachines* **2024**, *15*, 34.
[31] P. Fu, P.-N. Ni, B. Wu, X.-Z. Pei, Q.-H. Wang, P.-P. Chen, C. Xu, Q. Kan, W.-G. Chu, Y.-Y. Xie, *Adv. Mater.* **2023**, *35*, 2204286.
[32] K. L. Kavanagh, *Semicond. Sci. Technol.* **2010**, *25*, 024006.
[33] W.-T. Huang, K.-B. Hong, A.-C. Liu, H.-C. Wang, C.-H. Lin, C.-Y. Weng, C.-H. Chang, T.-S. Kao, Y.-H. Hong, S.-W. Chang, H.-C. Kuo, *J. Light. Technol.* **2024**, 3338, https://doi.org/10.1109/JLT.2024.3522087.
[34] T. He, Y. Meng, Z. Liu, F. Hu, R. Wang, D. Li, P. Yan, Q. Liu, M. Gong, Q. Xiao, *Opt. Express* **2021**, *29*, 39406.
[35] Y. Chen, Z. Lin, S. B. Villers, L. A. Rusch, W. Shi, *IEEE J. Sel. Top. Quantum Electron.* **2020**, *26*, 6100107.
[36] M. Zahid-y, Y. Liu, D. Cozzolino, Y. Ding, T. Morioka, L. K. Oxenløwe, D. Bacco, *Nanophotonics* **2022**, *11*, 821.
[37] H. Kim, W.-J. Lee, A. C. Farrell, J. S. D. Morales, P. Senanayake, S. V. Prikhodko, T. J. Ochalski, D. L. Huffaker, *Nano Lett.* **2017**, *17*, 3465.
[38] Z. Azimi, A. Gopakumar, L. Li, F. Kremer, M. Lockrey, A.-A. Wibowo, H. T. Nguyen, H. H. Tan, C. Jagadish, J. Wong-Leung, *Adv. Opt. Mater.* **2022**, *10*, 2200739.
[39] COMSOL Multiphysics®. www.comsol.com. COMSOL AB, Stockholm, Sweden.
[40] L.-H. Wu, X. Hu, *Phys. Rev. Lett.* **2015**, *114*, 223901.
[41] S. Han, J. Cui, Y. Chua, Y. Zeng, L. Hu, M. Dai, F. Wang, F. Sun, S. Zhu, L. Li, A. G. Davies, E. H. Linfield, C. S. Tan, Y. Kivshar, Q. J. Wang, *Light Sci. Appl.* **2023**, *12*, 145.
[42] J. Jin, X. Yin, L. Ni, M. Soljacic, B.o Zhen, C. Peng, *Nature* **2019**, *574*, 501.
[43] Z. Wang, Y. Liang, M. Beck, G. Scalari, J. Faist, *Phys. Rev. B* **2020**, *102*, 045122.
[44] M. Zhou, A. R. Kumar Kalapala, M. Pan, R. Gibson, K. J. Reilly, T. Rotter, G. Balakrishnan, R. Bedford, W. Zhou, S. Fan, *ACS Photonics* **2023**, *10*, 1519.
[45] A. S. L. Gomes, A. L. Moura, C. B. de Araújo, E. P. Raposo, *Prog. Quantum Electron.* **2021**, *78*, 100343.
[46] D. S. Wiersma, *Nat. Phys.* **2008**, *4*, 359.
[47] M. Lee, S. Callard, C. Seassal, H. Jeon, *Nat. Photonics* **2019**, *13*, 445.
[48] S. Nojima, H. Asahi, *J. Appl. Phys.* **1988**, *63*, 479.
[49] M. S. Alam, M. S. Rahman, M. R. Islam, A. G. Bhuiyan, M. Yamada, *IEEE 19th Int. Conf. Indium Phosphide & Related Mater.* **2007**, 343, https://doi.org/10.1109/ICIPRM.2007.381193.
[50] K. Papatryfonos, T. Angelova, A. Brimont, B. Reid, S. Guldin, P. R. Smith, M. Tang, K. Li, A. J. Seeds, H. Liu, D. R. Selviah, *AIP Adv.* **2021**, *11*, 025327.
[51] K. Luke, Y. Okawachi, M. R. E. Lamont, A. L. Gaeta, M. Lipson, *Opt. Lett.* **2015**, *40*, 4823.
[52] M. A. Green, *Sol. Energy Mater. Sol. Cells* **2008**, *92*, 1305.
[53] I. H. Malitson, *JOSA* **1965**, *55*, 1205.